RSC Advances

ROYAL SOCIETY OF CHEMISTRY

PAPER

View Article Online
View Journal | View Issue

Check for updates

Cite this: *RSC Adv.*, 2020, **10**, 12183

CuS nanoparticles anchored to g-C_3N_4 nanosheets for photothermal ablation of bacteria†

Xiaoyu Liu,‡[b] Xiaoyan Li, ‡*[a] Yan Shan,*[b] Yixin Yin,[c] Congrui Liu,[a] Ziyi Lin[a] and Supriya Soraiya Kumar[d]

Antibiotic resistance has already been recognized as one of the greatest threats to human beings' health, and thus it is highly desirable to develop new bactericidal approaches. The photothermal antibacterial process based on the photo-to-thermal conversion using semiconducting materials is currently extensively studied owing to its high efficiency, long durability and environmental benignity. In this study, we fabricated copper sulfide (CuS) nanoparticle-decorated graphitic carbon nitride (g-C_3N_4) nanosheets, denoted as the PEG-CuS@g-C_3N_4 nanocomposite, *via* a simple hydrothermal process. Materials characterization showed that CuS nanoparticles were uniformly distributed on the surface of g-C_3N_4 without agglomeration. Moreover, the nanocomposite exhibited excellent photothermal conversion efficiency (up to 59.64%) due to its strong near-infrared (NIR) absorption characteristics. The antibacterial efficiency evaluation indicated that the PEG-CuS@g-C_3N_4 nanocomposite could effectively kill the Gram-positive *Staphylococcus aureus* (*S. aureus*) and the Gram-negative *Escherichia coli* (*E. coli*). We found that up to 99% of both *S. aureus* and *E. coli* could be killed in a 200 μg ml^{-1} PEG-CuS@g-C_3N_4 suspension within 20 min of NIR irradiation. Moreover, the cytotoxicity of the PEG-CuS@g-C_3N_4 nanocomposite was evaluated using the mouse skin fibroblast NIH-3T3 cells, and the nanocomposite was found to display acceptable biocompatibility. We believe that the PEG-CuS@g-C_3N_4 nanocomposite is of significant interest for rapid bacteria-killing, and would gain promising applications for sterilization.

Received 18th January 2020
Accepted 15th March 2020

DOI: 10.1039/d0ra00566e

rsc.li/rsc-advances

1. Introduction

Microbial contamination has become a serious concern in various fields such as the medical, health care, food, cosmetics and environmental industries. As the most common infectious bacteria in our daily lives, *S. aureus* and *E. coli* profoundly affect public health, and are the main pathogens of numerous infectious diseases such as bacteremia, pneumonia, endocarditis, septic arthritis, osteomyelitis, and deep abscess formation.[1–4] In recent decades, diseases caused by bacterial infections have once again been recognized as one of the greatest threats to public health due to the emergence and rapid spread of bacterial resistance to available antibiotics.[5] To address the global crisis of antibiotic resistance, it is imperative to explore highly effective and scalable bactericides and antibacterial techniques that show lower tendencies to induce drug resistance.[6–9] In fact, numerous kinds of antibacterial materials and strategies have been developed in the past decades. For example, chemotherapies using antibacterial polypeptides,[10] noble metal nanoparticles (NPs),[11,12] semiconductor NPs[13,14] and carbon-based nanomaterials (CNMs)[15,16] were all proved to exhibit antimicrobial activities. More recently, photothermal or photodynamic sterilization techniques were extensively investigated in the eradication of bacteria *via* production of massive heating or the generation of reactive oxygen species.

Among these antimicrobial techniques, photothermal therapy (PTT)[17,18]-the combining of pulsed lasers with light-absorbing materials possessing high light-thermal conversion efficiency under the near infrared (NIR) laser irradiation, has attracted much research attention.[19] In short, the photothermal materials could efficiently absorb the energy from NIR photons and convert it into thermal energy. The generated heat then exterminated the antibiotic-resistant bacteria and subsequently prevented the formation of biofilm structures. Furthermore, with a wavelength between 700–1100 nm, NIR light has a high capability to penetrate deeper tissues with minimal damage to

---

[a] *Department of Endodontics, School and Hospital of Stomatology, Shandong University & Shandong Key Laboratory of Oral Tissue Regeneration & Shandong Engineering Laboratory for Dental Materials and Oral Tissue Regeneration, No.44-1 Wenhua Road West, 250012, Jinan, Shandong, China. E-mail: lixiaoyanwhu@sdu.edu.cn; Fax: +86-53188382923; Tel: +86-53188382624*

[b] *College of Materials Science and Engineering, Qingdao University of Science and Technology, No. 53 Zhengzhou Road, 266042, Qingdao, Shandong, China. E-mail: shanyan@qust.edu.cn*

[c] *Oral Implantology Center, Ji Nan Stomatology Hospital, No.101 Jingliu Road, 250001, Jinan, Shandong, China*

[d] *School of Basic Medical Sciences, Shandong University, No.44 Wenhua Road West, 250012, Jinan, Shandong, China*

† Electronic supplementary information (ESI) available. See DOI: 10.1039/d0ra00566e

‡ These authors contributed equally to this work.

healthy cells.[20–22] Therefore, PTT is regarded as a safe and efficient strategy to eliminate trapped bacteria. Carbon-based nanocomposites, metal nanomaterials, metallic compound nanocomposites and polymeric compounds are the most highly reported photothermal nanomaterials.[23] However, wide applications have been restricted by their inherent defects, such as poor biocompatibility, high cost, low photostability, tedious preparation procedures, and low targeting efficiency toward bacteria. Among these investigated materials, the copper sulfides (CuS)[18,19,24–30] stand out as suitable choices for photothermal therapy because of their excellent photothermal conversion efficiency in the NIR region and high intrinsic thermal conductivity.[31–33] However, the low surface area and easy sedimentation hindered their widely applications in PTT as a means of eliminating trapped bacteria. Therefore, it is highly desirable to modify the CuS NPs[17,34] to obtain a novel kind of multifunctional nanomaterials with high photothermal conversion efficiency, big loading capacity, slow sedimentation, low cost and easy fabrication.

As a stable, highly biocompatible chemical substance with the ability to absorb light efficiently in both visible and near-infrared ranges, 2-D structured polymeric carbon nitride (g-C_3N_4, PCN) can be easily synthesized, and has emerged as an attractive candidate for use as a platform for constructing hybrid materials. During the past few years, many research groups have reported different types of heterojunction photocatalysts comprised of g-C_3N_4 and metal oxides or sulphides showing improved photothermal conversion efficiencies when compared with their individual components.[32,35–39]

Inspired by the above efforts, we herein construct a self-assembled PTT agent, PEG-CuS@g-C_3N_4 by a rapid and simple recrystallization growth which was schematically illustrated in Scheme 1. In this composite, CuS played a role in generating hyperthermia under the NIR irradiation. g-C_3N_4 nanosheet served as a nano-scaffold of CuS preventing it from aggregating. The synthesized nanocomposite showed super photothermal conversion efficiency and excellent photothermal stability, indicating the PEG-CuS@g-C_3N_4 nanocomposite could be applied as a kind of promising photothermal agent for rapid sterilization. Importantly, PEG-CuS@g-C_3N_4 nanocomposite demonstrated acceptable toxicity to normal tissue cells.

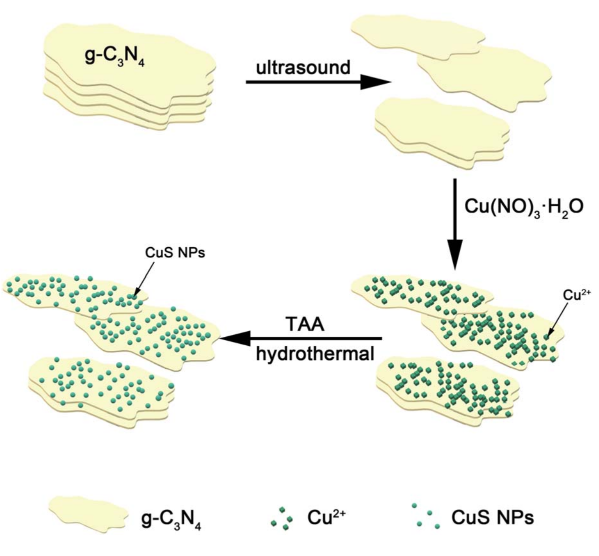

Scheme 1 Preparation process of CuS@g-C_3N_4 nanocomposite.

2. Experimental section

In this paper, CuS nanoparticles were assembled on the g-C_3N_4 nanosheets by hydrothermal process as detailed in the Experimental section.

2.1 Materials

All reagents for synthesis and analysis were commercially available and used without any further treatment. Thioacetamide (C_2H_5NS, ≥99.0%), urea (H_2NCONH_2, H_2NCONH_2, ≥99.0%) were purchased from Sinopharm Chemical Reagent Co., Ltd. Cupric nitrate ($Cu(NO_3)_2 \cdot 3H_2O$, ≥99.0–102%) was purchased from Hongyan Chemical Reagent Factory (Tianjin, China). Absolute ethanol (CH_3CH_2OH, ≥99.7%) was purchased from Fine Chemical Plant (Laiyang Economic and Technological Development Zone, China). Polyethylene glycol ($HO\ (CH_2CH_2O)_nH$) 2000 was purchased from Damao Chemical Reagent Factory (Tianjin, China). High purity water (18.2 MU cm) was obtained from a Milli-Q system (Millipore) and used in all the experiments.

2.2 Synthesis of g-C_3N_4 nanosheets

The polymeric g-C_3N_4 was prepared by simple pyrolysis of urea. Briefly, 10 g of urea powder was placed in an alumina crucible with a lid and dried at 80 °C. Then, the urea was heated to 500 °C from room temperature in the box-type muffle furnace with a heating rate of 5 °C min^{-1} and maintained at 500 °C for 3 h to produce the powdered g-C_3N_4.

2.3 Synthesis of PEG-CuS@g-C_3N_4 nanocomposite

In a typical synthesis, 0.3 g g-C_3N_4 was dispersed into 30 ml deionized water in a 100 ml beaker and ultrasonically oscillated for 30 min in order to get a single layer or several layers of g-C_3N_4, and then 0.252 g $Cu(NO_3)_2 \cdot 3H_2O$ and 0.075 g thioacetamide (TAA) were added slowly while stirring constantly. Afterward, the mixed solution was transferred into a 100 ml autoclave and heated at 160 °C for 6 h. After cooling to room temperature, the nanocomposite was collected by centrifugation (denoted as CuS@g-C_3N_4 nanocomposite) and then modified with PEG which helps to reduce the cytotoxicity of the nanocomposite described as PEG-CuS@g-C_3N_4 nanocomposite.

2.4 Characterizations

The crystal structure of the resultant products was characterized by X-ray diffraction (XRD, powder X-ray diffractometer with Cu-Kα radiation source, $\lambda = 1.5406$ Å). Morphologies of the materials were identified by a field emission scanning electron microscope (SEM, HITACHI regulus 8100) and a transmission electron microscope (TEM, JPN Thermo Fischer Talos F200x) at an acceleration voltage of 200 kV. The UV-vis spectra were obtained on UV-visible-spectrophotometer (UV-vis, UH4150). The UV-vis-NIR absorbance spectra of solution was obtained by UV-visible spectrometer (UV-vis, Evolution 201). Brunauer–Emmet–Teller (BET, a Kubo X1000 instrument) specific surface area (SSA) and pore size distribution (PSD) were obtained using a Quantachrome Autosorb-IQ2 instrument with nitrogen adsorption at 77 K using the Barrett–Joyner–Halenda (BJH) method.

2.5 Photothermal effects

Photothermal temperature test was measured by using laser and paperless recorder. Briefly, 300 μL of PEG-CuS@g-C_3N_4 nanocomposite solution (200 μg ml^{-1}) was exposed to a 808 nm laser at a power of 2.5 W for different time durations. The temperature of the solution was monitored using a DT-8891E thermocouple linked to a digital thermometer (MIK200D, Hangzhou Meikong Automation Technology Co., Ltd.).

2.6 Antibacterial activity test

Wide-type *E. coli* (ATCC 35218) and *S. aureus* (ATCC 25923) were employed as the models of Gram-negative and Gram-positive bacterium strains, respectively. Following activation and incubation, logarithmic growth phase bacterial was diluted 200-fold with fresh brain heart infusion (BHI) or lysogeny broth (LB) medium and supplemented with 200 μg ml^{-1} of PEG-CuS@C_3N_4 and then illuminated with laser (808 nm, 2.5 W) for different time durations (0, 5 and 20 min).

For CFU assay, the bacterial suspensions were diluted and then 10 μl of the bacterial dilutions was coated and incubated on BHI or LB agar plates with a spreader for overnight at 37 °C. Assessment of colony forming unit (CFU) quantization was implemented by arithmetic on the basis of CFUs emergence.

For the measurement of the survival rate of the strains, the bacterial suspensions were then stained for 15 min in the dark at room temperature with the ViaQuant™ Viability/Cytotoxicity Kit for Bacteria Cells (GeneCopoeia™) comprised of NucBeacon GREEN and propidium iodide (PI). The cells were imaged using a confocal laser scanning fluorescence microscope with 10 objective. Bacteria survival rate was calculated using the following equation:

$$\text{survival rate (\%)}\ C/C_0\ 100\%$$

where C_0 and C correspond to the proportions of live cells with the control C_3N_4 at $t = 0$ and the samples.

The morphology of *E. coli* and *S. aureus* after contact with the samples were observed by SEM with an accelerating voltage of 1.2 kV. The bacterial suspensions were first rinsed by using PBS. Then, they were fixed with paraformaldehyde at 4 °C for 30 min and dehydrated in graded ethanol series (30–100%). The suspension was dropped onto a clean silicon wafer and dried naturally, sputter-coated with platinum for SEM observation.

2.7 Cytotoxicity and measurements

Cytotoxicity induced by PEG-CuS@g-C_3N_4 nanocomposite was assessed by cell count kit-8 (CCK-8) and live/dead assays. Briefly, mouse skin fibroblast NIH-3T3 cells (obtained from the Cell Bank of Type Culture Collection, Chinese Academy of Sciences, Shanghai) were seeded on 96-well plates (Corning) at a density of 1×10^4 cells per well and cultured in complete culture medium containing 10% FBS. After 24 hours of incubation, the cells reached ~80% confluence. For our CCK-8 experiments, the cells were exposed to PEG-CuS@g-C_3N_4 at various concentrations (0–500 μg ml^{-1}) dispersed in the DMEM medium for 24 h. And then the culture medium was replaced with 100 μl of CCK-8 solution (containing 90 μl of serum-free DMEM and 10 μl of CCK-8 reagent) and subsequently incubated at 37 °C for 2 h. Absorbance of the CCK-8 solutions was measured using a microplate reader at a wavelength of 450 nm. The cytotoxicity of different samples was also determined by live/dead staining. Mouse skin fibroblast NIH-3T3 cells were seed on 24-well plates and exposed to PEG-CuS@g-C_3N_4. Next, the wells were rinsed *via* PBS for three times. Then, cells were treated with a mixture solution containing 1 mM FDA (live) and 2 mM propidium iodide (dead) in complete culture medium for 15 min and visualized by fluorescence microscope.

2.8 Statistics

The results are expressed as mean ± standard deviation. Standard deviation is indicated by the error bars. Student's *t*-test was used to determine significance among the small groups.

3. Results and discussion

3.1 Structure and morphology

As shown in Fig. 1a, XRD was used to characterize the crystal structures of pure g-C_3N_4, CuS and CuS@g-C_3N_4 composites. Two characteristic peaks of 12.9° and 27.4° in the pure g-C_3N_4 sample can be indexed to the (100) and (002) diffractions corresponding to the in-plane packing and interfacial stacking of aromatic systems, respectively. XRD pattern of pure CuS showed its wurtzite structure (PDF#79–2321). The peak at 29.3°, 31.8° and 47.9° corresponded to the (102), (103) and (110) diffraction peaks of CuS. The XRD pattern of CuS@g-C_3N_4 nanocomposite showed the sample had all the peaks of CuS and g-C_3N_4. When these inorganic and organic heterostructure are hybridized, the main characteristic diffraction peaks of the CuS@g-C_3N_4 are similar to those of the pure g-C_3N_4. Meanwhile typical crystalline of CuS apparently emerged in all CuS@g-C_3N_4 nanocomposite. The above results indicated CuS was successfully coupled with g-C_3N_4.

In order to investigate the details of the structure of CuS@g-C_3N_4 nanocomposite, scanning electron microscope (SEM) and transmission electron microscopy (TEM) was employed. As illustrated in Fig. S1,† the wrinkled lamellar structure with smooth surface can be observed clearly in the pure g-C_3N_4 sample. After introduction of the CuS to the g-C_3N_4 sample (Fig. 1b and c) the lamellar structure of g-C_3N_4 preserved and numerous of CuS are well-dispersed on the surface of g-C_3N_4. The microstructure of as-prepared samples was further investigated *via* TEM. TEM images show that a large amount of CuS nanoparticles are deposited on the surface of g-C_3N_4 with good

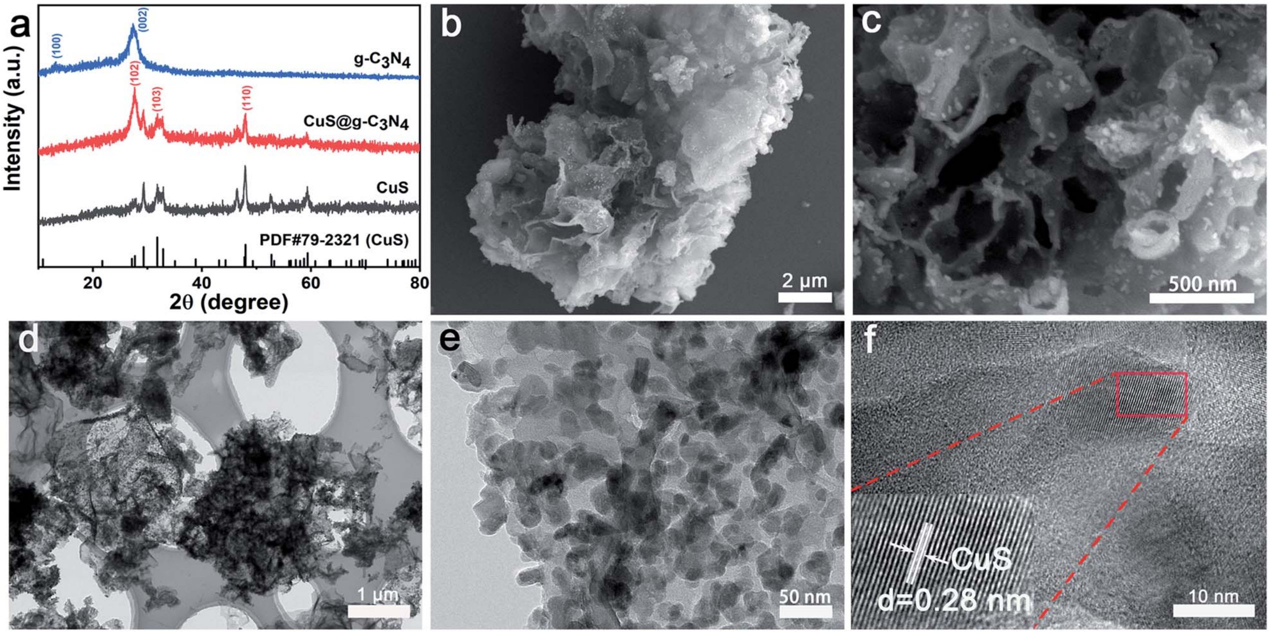

Fig. 1 (a) XRD patterns, (b and c) SEM images, (d and e) TEM images and (f) HR-TEM image of CuS@C_3N_4 composite.

dispersion (Fig. 1d and e). By HR-TEM observations, it was hard to find the corresponding lattice fringe of g-C_3N_4. The lattice fringes presented in Fig. 1f was 0.28 nm, which should be ascribed to CuS. This result indicated that g-C_3N_4@CuS nanocomposite was heterogeneous in structure rather than a mechanical mixture of two separate substances of g-C_3N_4 and CuS.

3.2 Photothermal measurement

The UV-vis absorption spectra were used to measure the optical absorption property of the g-C_3N_4, CuS and the CuS@g-C_3N_4 nanocomposite. As shown in Fig. 2a, the pristine g-C_3N_4 shows an absorption edge around 380 nm and the corresponding band gap was *ca.* ~2.7 eV. For pure CuS, it has a broad absorption range from visible light to near-infrared light and the corresponding band gap was about ~1.8 eV (Fig. 2b).

The temperature profiles of pure water, g-C_3N_4, CuS, CuS@g-C_3N_4 nanocomposite and PEG-CuS@g-C_3N_4 nanocomposite were performed by 808 nm laser irradiation. As illustrated in Fig. 2c, the temperature of PEG-CuS@g-C_3N_4 suspension (200 μg ml^{-1}) drastically increased with the irradiation time. It can be seen that the temperature variation (Δt, referring to the gap between the measured temperature and room temperature) of CuS@g-C_3N_4 and PEG-CuS@g-C_3N_4 were about 25 °C, which was higher than that of pure CuS ($\Delta t \approx 20$ °C), pure g-C_3N_4 ($\Delta t \approx 3$ °C) and deionized water ($\Delta t \approx 1$ °C), indicating the photo-to-thermal conversion efficiency on PEG-CuS@g-C_3N_4 was much improved compared to its mono-component counterparts. Besides, there was no statistically significant difference between CuS@g-C_3N_4 and PEG modified CuS@g-C_3N_4, indicated that PEG modification exert negligible affect on the photothermal efficiency.

The photothermal conversion efficiency, η, was calculated using eqn (1):

$$\eta = \frac{hs(T_{\mathrm{Max}} - T_{\mathrm{surr}}) - Q_{\mathrm{Dis}}}{I(1 - 10^{-A_{808}})} \tag{1}$$

where h is the heat transfer coefficient, s is the surface area of the container, and the value of hs is obtained from the Fig. 2c. T_{Max} is the highest equilibrium temperature, T_{surr} is the temperature of the surrounding, and ($T_{\mathrm{Max}} - T_{\mathrm{surr}}$) is 26.2 °C according to the Fig. 2d. Q_{Dis} is the heat dissipated which was absorbed by the quartz cell from laser, and it was measured independently to be 548.7 mW using a quartz cuvette cell containing pure water. I is the laser power which was stable at 2.5 W, A_{808} is the absorbance (1.27) of the sample solution at the excitation wavelength of 808 nm (Fig. S6†). The value of hs is derived according to the eqn (2):

$$\tau_{\mathrm{s}} = \frac{\sum_{\mathrm{i}} m_{\mathrm{i}} C_{\mathrm{pi}}}{hs} \tag{2}$$

In the eqn (2), τ_{s} is the sample system time constant, $m_{\mathrm{pure\ water}} = 0.3$ g, $m_{\mathrm{quartz\ tube}} = 1.23$ g, $C_{\mathrm{ppure\ water}} = 4.20$ J g^{-1}, $C_{\mathrm{pquartz}} = 0.07$ J g^{-1}, respectively. In Fig. 2e the slope of the plot of cooling time *versus* negative temperature logarithm obtained from the cooling stage is the time constant (τ_{s}), it could be calculated to be 163.58. Substitute the above parameters into eqn (1), the photothermal conversion efficiency of PEG-CuS@g-C_3N_4 nanocomposite under the 808 nm laser irradiation could be calculated as 59.64%. The photothermal conversion was relatively higher than that previously reported materials, such as CuS@DSPE-PEG nanoparticles (31.4%, 800 nm laser),[40] hollow CuS nanocubes (30.3%, 808 nm laser),[41] and CuS/SiO_2-

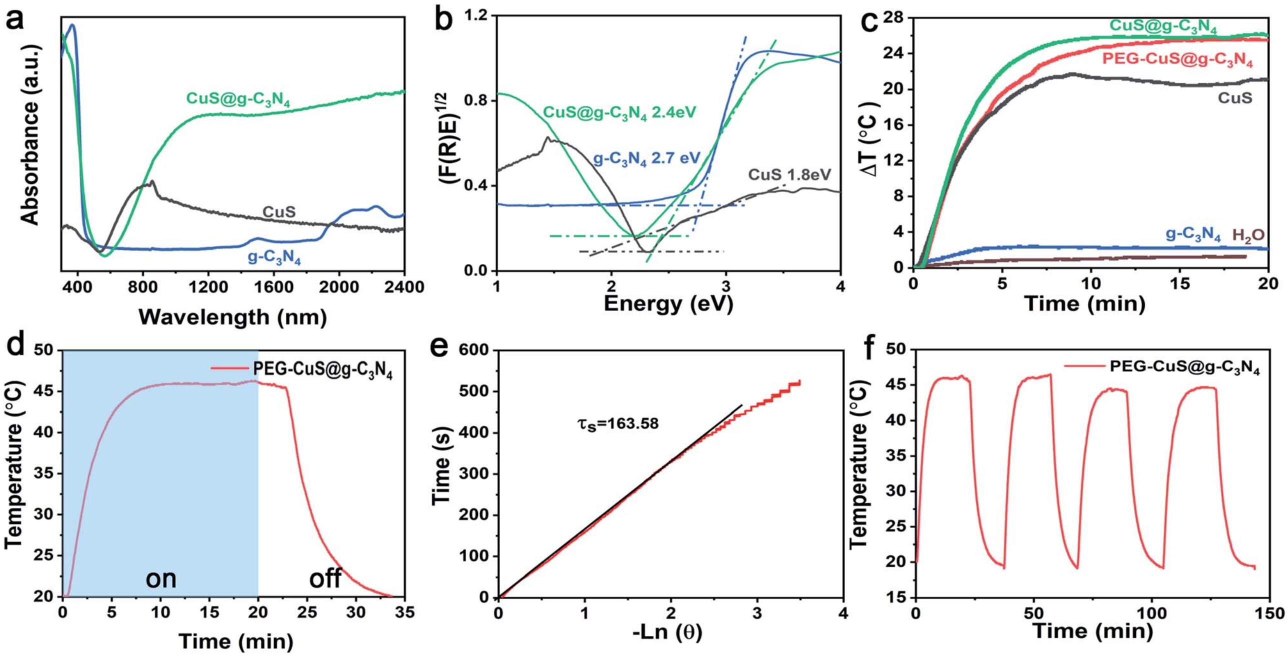

Fig. 2 (a) UV-vis absorption spectra, (b) plots of modified Kubelka–Munk function *versus* energy of light, (c) temperature profiles of pure water, g-C_3N_4, CuS, CuS@g-C_3N_4 nanocomposite and PEG modified CuS@g-C_3N_4 nanocomposite (200 μg ml^{-1}) as a function of irradiation time (0–20 min) under 808 nm laser irradiation, (d) photothermal effect of PEG-CuS@g-C_3N_4 nanocomposite (200 μg ml^{-1}) aqueous dispersion illuminated with an 808 nm laser for 20 min. The laser was turned off and sustained for 15 min, (e) plot of cooling time *versus* negative natural logarithm of the temperature driving force obtained from the cooling stage as shown in (c), and (f) temperature profiles of PEG-CuS@g-C_3N_4 nanocomposite suspension for four on–off cycles.

based nanotherapeutic agent (31.7%, 808 nm laser).[42] To investigate the photothermal stability of the PEG-CuS@g-C_3N_4 nanocomposite, four cycles of LASER ON/OFF experiments were conducted (Fig. 2f). The dispersion of the PEG-CuS@g-C_3N_4 nanocomposite was irradiated with 808 nm laser for 20 min (LASER ON), followed by naturally cooling to the room temperature (without irradiation, LASER OFF). After four cycles of LASER ON/OFF by the 808 nm laser, the PEG-CuS@g-C_3N_4 nanocomposite remained largely constant, which suggested that the PEG-CuS@g-C_3N_4 nanocomposite showed excellent photothermal stability. As indicated by the electron microscopy images, CuS were dispersed on the surface of sheet-like g-C_3N_4 and this structure could effectively prevent the agglomeration of CuS nanoparticles. The incident photon energy (808 nm) is below the bandgap of g-C_3N_4. The relaxation process of sub-band gap absorption has very little effect on the composition and the structure of the material. In addition, under NIR irradiation, the oxidizing ability of the generated holes in CuS is not strong enough due to the shallow S 3p bands. These super photothermal conversion efficiency and excellent photothermal stability make the PEG-CuS@g-C_3N_4 nanocomposite as promising recyclable photothermal agent.

3.3. Photothermal antibacterial assays

We studied the photothermal antibacterial assay using PEG-CuS@g-C_3N_4 nanocomposite under 808 nm laser irradiation (a commonly used light sources in PTT studies). To investigate the photothermal antibacterial effectiveness of the nanocomposite,

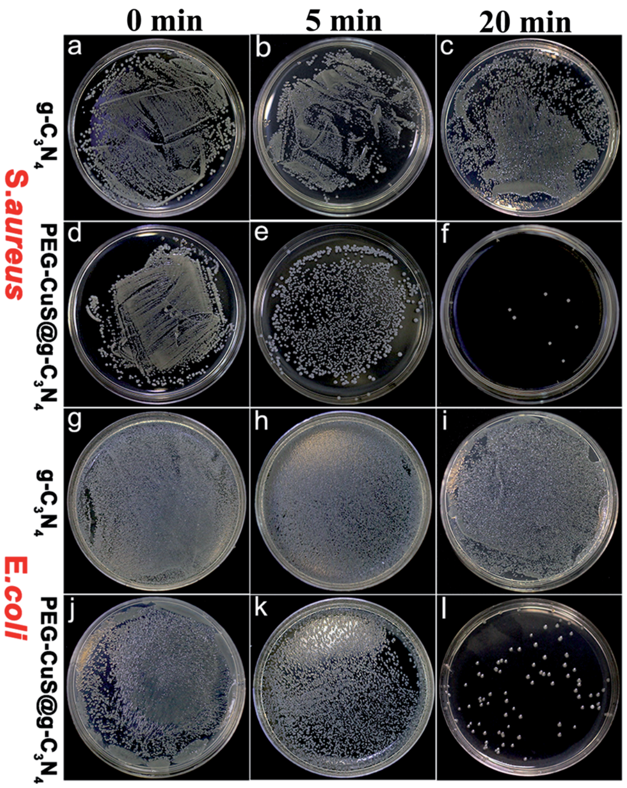

Fig. 3 CFU of *S. aureus* (a–f) on BHI agar plate and *E. coli* (g–l) on LB agar plate incubated with g-C_3N_4 or PEG-CuS@g-C_3N_4 with 808 nm laser irradiation.

CFUs in the different experiments were counted. Fig. 3f and l showed that the CFU values of PEG-CuS@g-C_3N_4 group were reduced by approximately 99% under 808 nm laser irradiation, for 20 min, which was due to the photothermal effect of PEG-CuS@g-C_3N_4 nanocomposite. However, the CFU values of g-C_3N_4 were not changed with time increasing after NIR irradiation (Fig. 3c and i), indicated that bacteria can survive after NIR irradiation. These results indicate that the PEG-CuS@g-C_3N_4 nanocomposite exhibited high bacterial inhibition capability upon NIR irradiation.

We further carried out a fluorescence-based cell viability assay to verify the bacteria survival rate. Membrane-impermeant propidium iodide (PI) labels dead bacteria with red fluorescence, whereas NucBeacon GREEN labels live bacteria with green fluorescence. For *S. aureus* and *E. coli*, as shown in Fig. 4a, d, g and j, there was almost no dead bacteria observed under dark suggesting that neither of the two bacteria strains were affected by g-C_3N_4 or PEG-CuS@g-C_3N_4 nanocomposite. After the NIR irradiation, the number of dead bacteria increased with time for PEG-CuS@g-C_3N_4 group. At 20 min, more than 95% of the bacteria died (Fig. 4f and l), which was corresponding to Fig. 3. The control group (Fig. 4c and i) showed only green dots, indicating that no bacteria apoptosis or death occurred in this case. The bacteria survival rate was further verified. As shown in Fig. 4m (*S. aureus*) and Fig. 4n (*E. coli*), few *S. aureus* and *E. coli* were inactivated with C_3N_4 under 20 min NIR irradiation. But with the presence of PEG-CuS@g-C_3N_4 nanocomposite, the survival rate was decreased within 5 min (67% for *S. aureus* and 64% for *E. coli*). Moreover, by prolonging the exposure time to 20 min, a disinfection efficiency of 98% for *S. aureus* and 95% for *E. coli* can be achieved.

To further analyze the antibacterial behavior, SEM was used to investigate cellular morphological changes of *S. aureus* and *E. coli*. As shown in Fig. 5, bacterial showed the perfect sphere-shaped (Fig. 5a and d) or rod-shaped (Fig. 5g and j) morphology with smooth surface before treatment. After treatment with NIR irradiation, for 5 min, some disruptions occurred on the cellular membrane, cell walls became partially wrinkled and incomplete (Fig. 5e and k) for PEG-CuS@g-C_3N_4 group. Notably, after treatment for 20 min with NIR irradiation, the bacterial surfaces showed much more violent damage. Cell membrane disrupted and leakage of intracellular material leading to cell death (Fig. 5f and l). The control group (Fig. 4c and i) remained perfect morphology with smooth surface after treatment for 20 min with NIR irradiation. All the results of the SEM images agreed well with the results of bacterial live-dead staining.

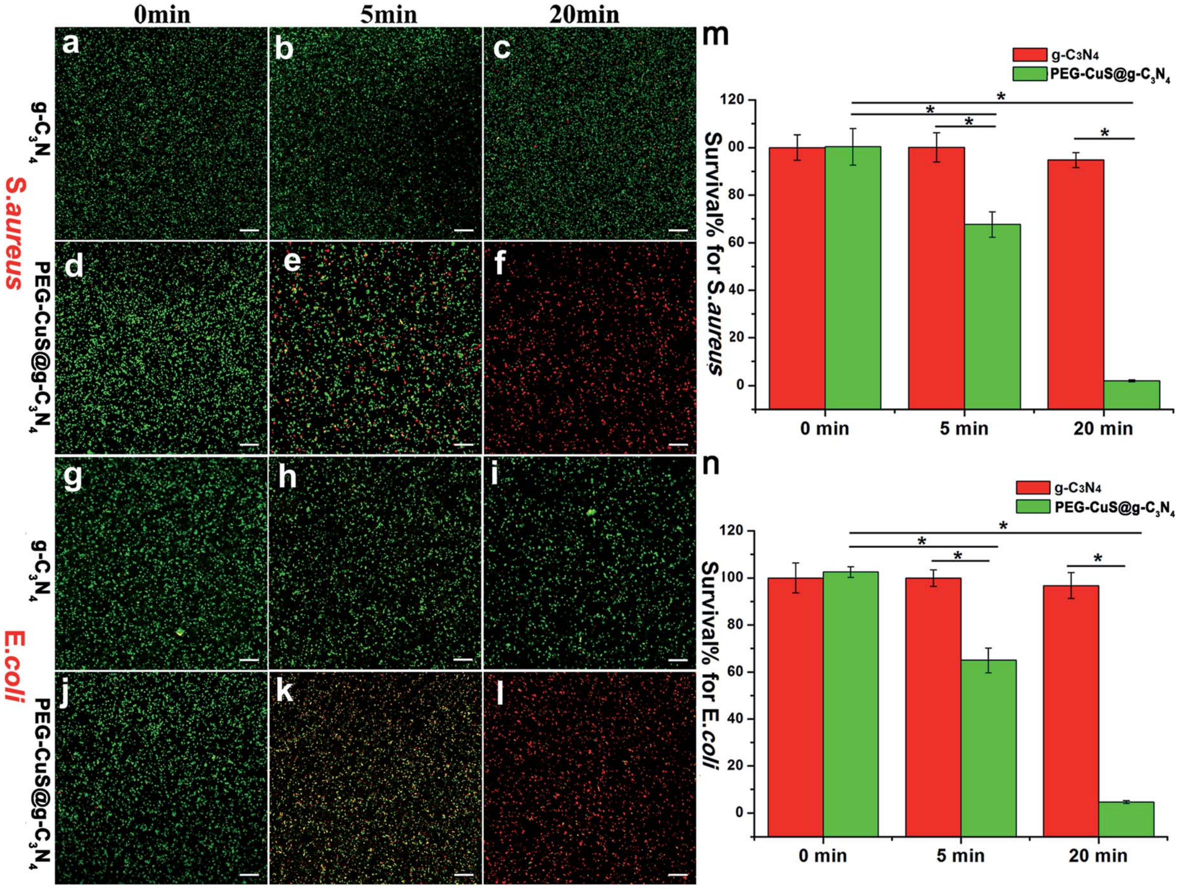

Fig. 4 Confocal fluorescent images of live or dead *S. aureus* (a–f) and *E. coli* (g–l) treated with 200 μg ml^{-1} of g-C_3N_4 or PEG-CuS@g-C_3N_4 suspensions in different time intervals stained with NucBeacon Green (green) and PI (red), scale bar is 50 μm. (m and n) Bactericidal efficiency at different laser irradiation time as indicated by the survival rate, statistically significant difference ($p < 0.05$). Three independent experiments were performed for each group.

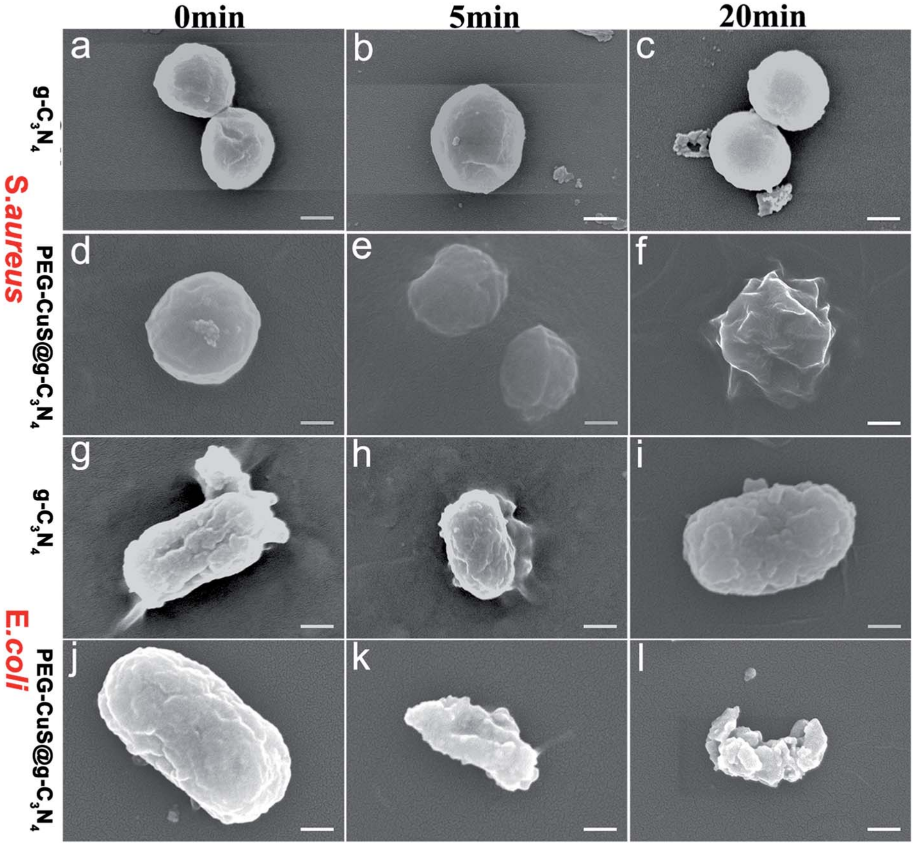

Fig. 5 SEM images of *S. aureus* (a–f) and *E. coli* (g–l) treated with g-C_3N_4 or PEG-CuS@g-C_3N_4 suspensions (200 μg ml^{-1}) under NIR, scale bar is 200 nm.

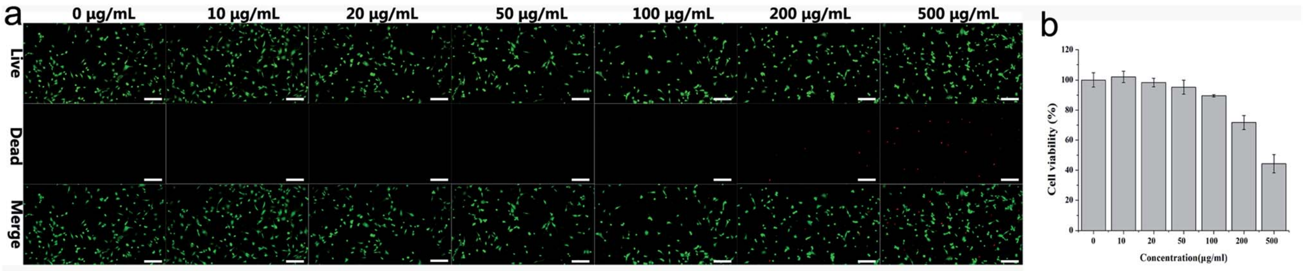

Fig. 6 Cytotoxicity of PEG-CuS@g-C_3N_4 in mouse skin fibroblast NIH-3T3 cells as determined by live/dead staining (a) and CCK8 assay (b), scale bar is 200 μm.

3.4 *In vitro* cell cytotoxicity study

The cytotoxicity of PEG-CuS@g-C_3N_4 nanocomposite was evaluated in mouse skin fibroblast NIH-3T3 cells by LIVE/DEAD Viability/Cytotoxicity Kit and Cell Count Kit-8 (CCK-8). As shown in Fig. 6a, there were almost no dead cells observed within 24 h until the concentration of suspension reached 100 μg ml^{-1}. The number of dead cells increased when the concentration of the material reached 200 μg ml^{-1}.

CCK8 was carried out to further investigate the effects of PEG-CuS@g-C_3N_4 nanocomposite on the viability of the mouse skin fibroblast NIH-3T3 cells (Fig. 6b). In consideration of copper release after 24 h cultivation, the sample possessed certain degree of inhibition to the cell growth. However, compared to control sample, there was almost no significant toxicity until the concentration of suspension reached 100 μg ml^{-1} within 24 h. When the concentration of the material reached 200 μg ml^{-1}, there were still numerous cells that survived and grew after treatment and the cell viability is above 70% considering non-cytotoxic according to ISO10993. These results revealed the PEG-CuS@g-C_3N_4 nanocomposite exhibited the acceptable biocompatibility.

4. Conclusions

In conclusion, the PEG-CuS@g-C_3N_4 nanocomposite was successfully fabricated *via* a simple hydrothermal synthesis pathway. Materials characterizations showed that CuS nanoparticles uniformly distributed on the surface of g-C_3N_4 without agglomeration. The PEG-CuS@g-C_3N_4 nanocomposite displayed superb photothermal properties, which can be used as a novel photothermal agent. When exposed to 808 nm laser irradiation for 20 min, hyperthermia from PEG-CuS@g-C_3N_4 nanocomposite could effectively kill *E. coli* (Gram-negative) and *S. aureus* (Gram positive) cells, respectively. Additionally, the nanocomposite showed acceptable effect on cell growth in contact with the mammalian cells even after 24 h of incubation. Therefore, this functionalized nanocomposite may find great potential applications as a robust and effective sterilization for microbial contamination environment.

Authors' contributions

Xiaoyan Li designed and performed most of the biological experiment, interpreted the experimental results, and drafted the manuscript. Yan Shan designed the materials science experiment. Xiaoyu Liu performed most of the materials science experiment, collected and analyzed parts of data. Yixin Yin, Congrui Liu and Ziyi Lin performed some of the experiments. Supriya Soraiya Kumar revised the manuscript. All authors approved the final version of the manuscript.

Conflicts of interest

There are no conflicts to declare.

Acknowledgements

This work was supported by Medical and Health Science and Technology Development Project of Shandong Provincial (2018WSA01018); Dean's Research Assistance Foundation of Ji Nan Stomatology Hospital (2018-02).

References

1 R. Geneau, P. Lehoux, R. Pineault and P. Lamarche, *BMC Fam. Pract.*, 2008, **9**, 1–10.
2 J. Edelsberg, D. Weycker, R. Barron, X. Li, H. Wu, G. Oster, S. Badre, W. J. Langeberg and D. J. Weber, *Diagn. Microbiol. Infect. Dis.*, 2014, **78**, 255–262.
3 J. T. Poolman and A. S. Anderson, *Expert Rev. Vaccines*, 2018, **17**, 607–618.
4 J. Barros, L. D. R. Melo, P. Poeta, G. Igrejas, M. P. Ferraz, J. Azeredo and F. J. Monteiro, *Int. J. Antimicrob. Agents*, 2019, **54**, 329–337.
5 T. T. Yoshikawa, *J. Am. Geriatr. Soc.*, 2003, **50**, 226–229.
6 L. Jia, J. Qiu, L. Du, Z. Li, H. Liu and S. Ge, *Nanomedicine*, 2017, **12**, 761–776.
7 Q. You, Q. Sun, J. Wang, X. Tan, X. Pang, L. Liu, M. Yu, F. Tan and N. Li, *Nanoscale*, 2017, **9**, 3784–3796.
8 J. Fang, P. Zhang, H. Chang and X. Wang, *Sol. Energy Mater. Sol. Cells*, 2018, **185**, 456–463.
9 C. Liu, D. Kong, P. C. Hsu, H. Yuan, H. W. Lee, Y. Liu, H. Wang, S. Wang, K. Yan, D. Lin, P. A. Maraccini, K. M. Parker, A. B. Boehm and Y. Cui, *Nat. Nanotechnol.*, 2016, **11**, 1098–1104.
10 J. D. Steckbeck, B. Deslouches and R. C. Montelaro, *Expert Opin. Biol. Ther.*, 2014, **14**, 11–14.
11 X. Fan, F. Yang, C. Nie, Y. Yang, H. Ji, C. He, C. Cheng and C. Zhao, *ACS Appl. Mater. Interfaces*, 2018, **10**, 296–307.
12 C. M. Lakhani, B. T. Tierney, A. K. Manrai, J. Yang, P. M. Visscher and C. J. Patel, *Physiol. Behav.*, 2019, **176**, 139–148.
13 C. Regmi, D. Dhakal and S. W. Lee, *Nanotechnology*, 2018, **29**, 064001.
14 L. Wang, X. Zhang, X. Yu, F. Gao, Z. Shen, X. Zhang, S. Ge, J. Liu, Z. Gu and C. Chen, *Adv. Mater.*, 2019, **31**, 1901965.
15 N. Levi-Polyachenko, C. Young, C. MacNeill, A. Braden, L. Argenta and S. Reid, *Int. J. Hyperthermia*, 2014, **30**, 490–501.
16 G. Wang, H. Feng, L. Hu, W. Jin, Q. Hao, A. Gao, X. Peng, W. Li, K. Y. Wong, H. Wang, Z. Li and P. K. Chu, *Nat. Commun.*, 2018, **9**, 2055–2067.
17 Z. Yuan, S. Qu, Y. He, Y. Xu, L. Liang, X. Zhou, L. Gui, Y. Gu and H. Chen, *Biomater. Sci.*, 2018, 18–22.
18 B. Zhou, J. Zhao, Y. Qiao, Q. Wei, J. He, W. Li, D. Zhong, F. Ma, Y. Li and M. Zhou, *Applied Materials Today*, 2018, **13**, 285–297.
19 C. Xia, D. Xie, L. Xiong, Q. Zhang, Y. Wang, Z. Wang, Y. Wang, B. Li and C. Zhang, *RSC Adv.*, 2018, **8**, 27382–27389.
20 R. Weissleder, *Nat. Biotechnol.*, 2001, **19**, 316–317.
21 W. Sun, Y. Han, Z. Li, K. Ge and J. Zhang, *Langmuir*, 2016, **32**, 9237–9244.
22 A. C. V. Doughty, A. R. Hoover, E. Layton, C. K. Murray, E. W. Howard and W. R. Chen, *Materials*, 2019, **12**, 779–793.
23 J. W. Xu, K. Yao and Z. K. Xu, *Nanoscale*, 2019, **11**, 8680–8691.
24 C. Wu, X. Zhang, Z. Xia, M. Shu, H. Li, X. Xu, R. Si, A. I. Rykov, J. Wang, S. Yu, S. Wang and G. Sun, *J. Mater. Chem. A*, 2019, **7**, 14001–14010.
25 X. Liu, Q. Wang, C. Li, R. Zou, B. Li, G. Song, K. Xu, Y. Zheng and J. Hu, *Nanoscale*, 2014, **6**, 4361–4370.
26 C. X. Huang, H. J. Chen, F. Li, W. N. Wang, D. D. Li, X. Z. Yang, Z. H. Miao, Z. B. Zha, Y. Lu and H. S. Qian, *J. Mater. Chem. B*, 2017, **5**, 9487–9496.
27 X. Deng, K. Li, X. Cai, B. Liu, Y. Wei, K. Deng, Z. Xie, Z. Wu, P. Ma, Z. Hou, Z. Cheng and J. Lin, *Adv. Mater.*, 2017, **29**, 1–9.
28 J. Huang, J. Zhou, J. Zhuang, H. Gao, D. Huang, L. Wang, W. Wu, Q. Li, D. P. Yang and M. Y. Han, *ACS Appl. Mater. Interfaces*, 2017, **9**, 36606–36614.
29 J. Fu, J. Zhang, S. Li, L. Zhang, Z. Lin, L. Liang, A. Qin and X. Yu, *Mol. Pharm.*, 2018, **15**, 4621–4631.
30 H. Shi, R. Yan, L. Wu, Y. Sun, S. Liu, Z. Zhou, J. He and D. Ye, *Acta Biomater.*, 2018, **72**, 256–265.
31 Y. Zheng, Y. Liang, D. Zhang, Z. Zhou, J. Li, X. Sun and Y. N. Liu, *Chem. Commun.*, 2018, **54**, 13805–13808.
32 A. Curcio, A. K. A. Silva, S. Cabana, A. Espinosa, B. Baptiste, N. Menguy, C. Wilhelm and A. Abou-Hassan, *Theranostics*, 2019, **9**, 1288–1302.
33 Z. Zhang, X. Zhang, Y. Ding, P. Long, J. Guo and C. Wang, *Macromol. Biosci.*, 2019, **19**, 1–10.

34 B. Zhang, Y. Shan and K. Chen, *Mater. Chem. Phys.*, 2017, **193**, 82–88.

35 X. Li, Y. Li, G. Sun, N. Luo, B. Zhang and Z. Zhang, *Nanomaterials*, 2019, **9**, 724–740.

36 J. X. Sun, Y. P. Yuan, L. G. Qiu, X. Jiang, A. J. Xie, Y. H. Shen and J. F. Zhu, *Dalton Trans.*, 2012, **41**, 6756–6763.

37 Y. Zhang, Y. Liu, R. Li, M. Saddam Khan, P. Gao, Y. Zhang and Q. Wei, *Sci. Rep.*, 2017, **7**, 1–8.

38 S. H. Liu and W. X. Lin, *J. Hazard. Mater.*, 2019, **368**, 468–476.

39 H. T. Huu, X. D. N. Thi, K. N. Van, S. J. Kim and V. Vo, *Materials*, 2019, **12**, 1730–1747.

40 Y. Huang, Y. Lai, S. Shi, S. Hao, J. Wei and X. Chen, *Chem. - Asian J.*, 2015, **10**, 370–376.

41 M. Li, Y. Wang, H. Lin and F. Qu, *Mater. Sci. Eng., C*, 2019, **96**, 591–598.

42 X. Liu, T. Yang, Y. Han, L. Zou, H. Yang, J. Jiang, S. Liu, Q. Zhao and W. Huang, *ACS Appl. Mater. Interfaces*, 2018, **10**, 31008–31018.